Gradient Field Detection Using Interference of Stimulated Microwave Optical Sidebands

Kaleb Campbell,[1,2,*] Ying-Ju Wang,[3] Igor Savukov[4] Peter D. D. Schwindt[1] Yuan-Yu Jau,[1] and Vishal Shah[3]

[1]Sandia National Laboratory, 1515 Eubank SE, Albuquerque, New Mexico 87123, USA

[2]Center for Quantum Information and Control, Department of Physics and Astronomy, University of New Mexico, Albuquerque, New Mexico 87131, USA

[3]QuSpin Inc, 331S 104th St. Unit 130, Louisville, Colorado 80027, USA

[4]Los Alamos National Laboratory, Los Alamos, New Mexico 87545, USA

We demonstrate that stimulated microwave optical sideband generation using parametric frequency conversion can be utilized as a powerful technique for coherent state detection in atomic physics experiments. The technique has advantages over traditional absorption or polarization rotation-based measurements and enables the isolation of signal photons from probe photons. We outline a theoretical framework that accurately models sideband generation using a density matrix formalism. Using this technique, we demonstrate a novel intrinsic magnetic gradiometer that detects magnetic gradient fields between two spatially separated vapor cells by measuring the frequency of the beat note between sidebands generated within each cell. The sidebands are produced with high efficiency using parametric frequency conversion of a probe beam interacting with ^{87}Rb atoms in a coherent superposition of magnetically sensitive hyperfine ground states. Interference between the sidebands generates a low-frequency beat note whose frequency is determined by the magnetic field gradient between the two vapor cells. In contrast to traditional gradiometers the intermediate step of measuring the magnetic field experienced by the two vapor cells is unnecessary. We show that this technique can be readily implemented in a practical device by demonstrating a compact magnetic gradiometer sensor head with a sensitivity of 25 fT/cm/$\sqrt{\text{Hz}}$ with a 4.4 cm baseline, while operating in a noisy laboratory environment unshielded from Earth's field.

Atomic physics experiments generally rely on absorption or polarization rotation measurements for coherent state detection [1,2]. In this Letter, we show that hyperfine coherence can also be detected with high efficiency using parametric frequency conversion [3] to generate microwave optical sidebands. Depending on the optical depth of the atomic medium and detuning of the probe beam, up to 50% of the incoming probe photons can be converted into sideband (signal) photons. Unlike absorption and polarization rotation-based measurements, the frequency separation between the probe and sideband photons allows the sideband to be isolated with a frequency discriminator. In addition, in some configurations governed by selection rules, the optical polarization of the probe and sideband photons is orthogonal with respect to each other, allowing them to be easily separated with a polarizer.

Here we focus on an application in which we demonstrate an intrinsic optically pumped magnetic gradiometer that directly measures the magnetic gradient field between two spatially separated alkali vapor cells. Most optically pumped gradiometers rely on subtracting the output of two spatially separated optically pumped magnetometers (OPMs [4–7]) (synthetic gradiometer [8–11]), and differences and drifts between the two magnetometers can reduce the rejection of common mode signals.

In superconducting quantum interference device (SQUID) [12] magnetic sensors, an intrinsic gradiometer can be formed by connecting two spatially separated flux pickup coils with opposing polarities [13,14]. In contrast, few OPM-based techniques exist to build similar intrinsic gradiometers using vapor cells [15–19]. Our technique yields high resolution signals and can be utilized in a practical device in the Earth's magnetic field. The sideband
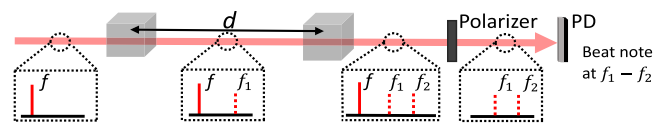

FIG. 1. (a) Conceptual overview of the gradiometer. Two alkali vapor cells are separated by a distance, d. A linear probe (carrier) beam with frequency f passes through the two vapor cells. The probe beam's interaction with the atoms in cell 1 produces an orthogonally polarized optical sideband at magnetic-field-dependent frequency f_1. Similarly, interaction with cell 2 produces a second optical sideband, at frequency f_2. The probe beam is removed using a polarizer, leaving behind only the two optical sidebands. The sidebands are captured by a photodetector (PD) where they interfere to produce a beat note at frequency $f_1 - f_2$ that is directly proportional to the magnetic gradient field between the two vapor cells.

generation technique can be adopted for a number of different applications such as biomagnetic field sensing [20–23], timing [24,25], and microwave detection [26,27], particularly in applications where separating a weak signal from a background probe is beneficial.

A conceptual overview of our gradiometer is shown in (Fig. 1). The sideband generation process is inspired by experiments performed in the 1970s, which showed that alkali atoms prepared in a coherent superposition of hyperfine ground states can modulate a weak probe (carrier) beam in a process known as parametric frequency conversion [3,28]. The time-dependent phase of the atomic coherence oscillates at the hyperfine resonance frequency, modulating the optical susceptibility of the atomic medium for near resonance light. When the atoms are probed by a weak beam, the oscillating susceptibility gives rise to both amplitude and phase modulation to generate optical sidebands.

We use the $5s^2 S_{1/2} |F = 1, m_F = 1\rangle = |1, 1\rangle$ and $|F = 2, m_F = 2\rangle = |2, 2\rangle$ ground state sublevels in a warm ensemble of ^{87}Rb as the basis for the gradiometer. Figure 2(a) shows our tabletop experimental setup demonstrating sideband generation. A cubic vapor cell with internal dimensions of $8 \times 8 \times 8$ mm^3 is filled with enriched ^{87}Rb and 30 Torr of nitrogen (N$_2$) buffer gas to minimize depolarization from cell wall collisions and to limit radiation trapping [29], which limits efficient optical pumping [30]. The vapor cell is exposed to a background magnetic field **B**, along the $\hat{z}$ direction. A circularly polarized (σ^+) 795 nm laser tuned to the $5s^2 S_{1/2} \to 5p^2 P_{1/2}$ $D1$ line, also along the $\hat{z}$ direction, optically pumps over 95% of the atoms into the $|2, 2\rangle$ "dark" state.
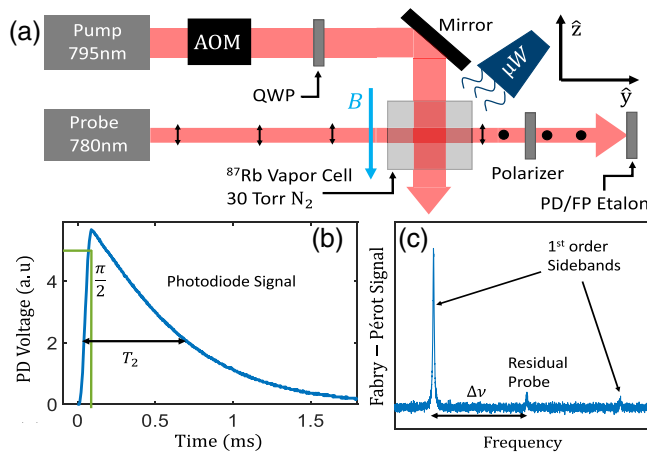

FIG. 2. (a) Experimental setup to observe sideband generation. Quarter wave plate (QWP). Microwave horn (μW). Acousto-optic modulator (AOM). (b) An example of a sideband measured with the PD. The decoherence time is denoted as T_2. (c) PD is replaced with a Fabry-Perot etalon to verify probe or sideband extinction depending on polarizer angle. The sideband that forms a resonant Λ system with the probe is stronger. The sideband relative amplitude dependence on probe detuning is shown in Fig. 3(b).

As the pumping approaches equilibrium, the pump light is switched off and the vapor cell is irradiated with a short (30 μs) microwave $\pi/2$ pulse using a microwave horn to prepare the atoms in a coherent supperposition of the $|1, 1\rangle \leftrightarrow |2, 2\rangle$ hyperfine ground states. A linearly polarized 780 nm laser (probe) tuned near the $|F = 1\rangle = |1\rangle \to 5p^2 P_{3/2}$ D2 line propagates through the vapor cell in a direction orthogonal to the pump. The interaction between the probe and the coherently prepared atoms generates an optical sideband near the $|F = 2\rangle = |2\rangle \to 5p^2 P_{3/2}$ transition. Sideband generation begins immediately after the $\pi/2$ pulse is applied, and its amplitude exponentially decays on a timescale T_2, the ground state coherence lifetime of the rubidium atoms in the vapor cell [Fig. 2(b)]. The generated first-order sideband(s) have linear polarization which is orthogonal with respect to the probe (carrier). The polarization orthogonality allows the probe and sidebands to be easily separated with a simple polarizer and analyzed independently. This was explicitly verified by replacing the photodiode with a scanning Fabry-Perot (FP) etalon [Fig. 2(c)] and extinguishing the probe and sidebands selectively by rotating the polarizer by a 90° offset angle.

Sideband generation is dependent on several parameters such as the degree of spin polarization, buffer gas pressure, probe detuning from resonance, and rubidium density (vapor cell temperature). Experimental observations of parameter dependency closely match predictions from our theoretical model described below. Under optimal conditions, the sideband amplitude is roughly equal to the probe amplitude after the beam exits the vapor cell. We found between 10 and 30 Torr of nitrogen buffer gas pressure to be ideal for sideband generation for our vapor cell dimensions. Pressure broadening [31] of the $5p^2 P_{3/2}$ excited state due to buffer gas at pressures higher than 30 Torr causes off-resonant excitation of the $|2\rangle$ state by the probe which reduces sideband generation efficiency, while buffer gas pressure lower than 10 Torr increases ground state relaxation through rubidium collisions with the vapor cell walls. The temperature of the vapor cell is adjusted to obtain a rubidium optical depth (OD) ≈ 1. In experiments at OD > 1, the probe is detuned from $|2\rangle \to |5p^2 P_{3/2}\rangle$ to maximize sideband generation.

The frequency difference between the sideband and the probe $\Delta \nu$ in low magnetic field is given by

$$\Delta \nu = \Delta \nu_{\text{HFS}} + \nu_{\text{BG}} + 3\gamma |\mathbf{B}|, \quad (1)$$

where $\Delta \nu_{\text{HFS}}$ is the separation between the two hyperfine ground states $|1\rangle$ and $|2\rangle$, ν_{BG} is the buffer gas induced pressure shift between the ground states, γ is the gyromagnetic ratio ($2\pi \times 6.99$(Hz/nT)), and $|\mathbf{B}|$ is the absolute background magnetic field experienced by the vapor cell. The dependence of the difference frequency, $\Delta \nu$, on the

magnetic field is amplified by a factor of three by probing the $|1,1\rangle \leftrightarrow |2,2\rangle$ hyperfine ground states.

To quantitatively analyze the experimental results, we developed a numerical model to simulate the sideband generation phenomena shown in Fig. 2. Using the previously developed theoretical framework described in an unpublished manuscript [32], or Chap. 8, in Ref. [33], we find an equation for a forward-propagated electric field through an atomic medium with multifrequency components as

$$\frac{\partial \tilde{\mathbf{E}}(\zeta)}{\partial \zeta} = -i\mathbf{K} \cdot \left(\mathbf{1} + \frac{\boldsymbol{\chi}}{2}\right) \cdot \tilde{\mathbf{E}}(\zeta), \qquad (2)$$

where ζ is the propagation distance through the medium in the direction of the probe, $\mathbf{K}$ is a k-vector dyadic operator (second order tensor), $\mathbf{1}$ is the unit dyadic, $\boldsymbol{\chi}$ is the electric susceptibility dyadic operator under the assumption $|\boldsymbol{\chi}| \ll 1$, and $\tilde{\mathbf{E}}(\zeta)$ is the frequency-quantized, complex position dependent electric field. A derivation of the propagation equation is given in the Supplemental Material [34], as well as an explanation of the matrix elements of the multifrequency dyadics shown in Eq. (2).

In the model, we use the two stretched ground-state hyperfine levels, $|1,1\rangle$ and $|2,2\rangle$. The other ground state sublevels have insignificant contributions to the sideband generation process if the optical pumping is efficient. One can think of the sideband generation process as stimulated Raman transitions between ground and excited states, forming a Λ system with an incident photon and a stimulated photon. For the experimental configuration of a linearly polarized probe which has its propagation direction orthogonal to the magnetic field, σ^{+}, σ^{-}, and π transition can occur. Figure 3(a) shows a possible Λ configuration for the negative frequency sideband, with two other configurations shown in the inset. The probe makes the transitions $|1,1\rangle \xrightarrow{\sigma^{+}} |2',2\rangle \xrightarrow{\pi} |2,2\rangle$, $|1,1\rangle \xrightarrow{\pi} |2',1\rangle \xrightarrow{\sigma^{-}} |2,2\rangle$, and $|1,1\rangle \xrightarrow{\pi} |1',1\rangle \xrightarrow{\sigma^{-}} |2,2\rangle$ where the prime indicates the excited state. For a first order effect, a probe photon (σ polarization) is scattered into the first order sideband (π polarization), which is orthogonal to the probe polarization.

Using the setup shown in Fig. 2(a), we send the light to a scanning FP etalon, and the amplitudes of the first order sidebands and probe light are measured. In Fig. 3(b), we experimentally scan the frequency of the probe across the $|1\rangle$ and $|2\rangle$ resonances, measuring the amplitude of the sidebands, and results from our numerical model are plotted with the experimental data. In the model, we calculate the propagation of the sideband through the medium at the number density 3.2×10^{12} cm^{-3} and determine the sideband amplitudes at the exit of the cell. Plots of sideband propagation as a function of distance are shown in the Supplemental Material [34]. The amplitude of the sideband and probe light is severely reduced on resonance
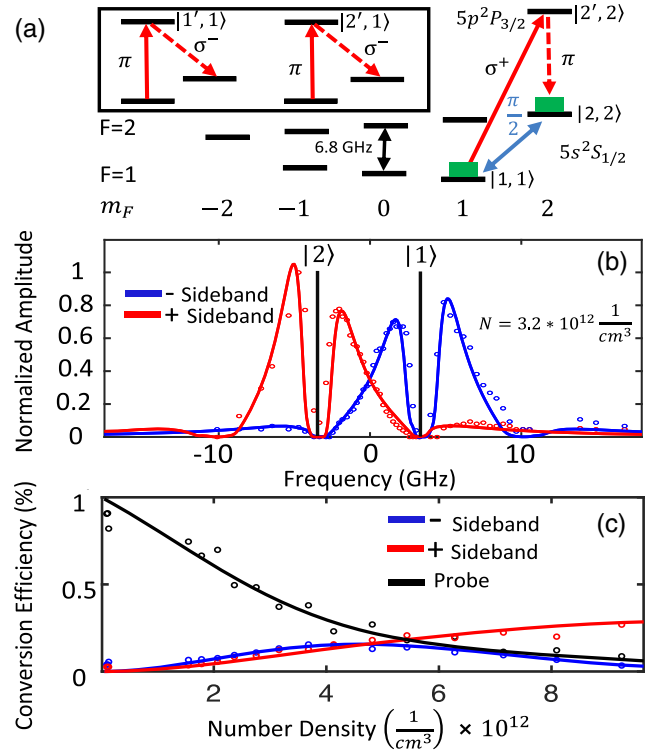

FIG. 3. (a) Ground state manifold of ^{87}Rb with transitions to an allowable excited state level. An example of a Λ system needed for sideband generation is shown. (b) First order sideband amplitude as the probe frequency is swept across transitions from the $|2\rangle$ and $|1\rangle$ states, with zero frequency halfway between the two resonances. The open circles are experimental data, and the solid lines are from the numerical model, which is qualitatively fit to the experimental data from the FP etalon. (c) Probe and sideband amplitude as a function of rubidium density.

due to absorption by the atoms. Also of note, if the probe frequency is set outside of either resonance by the hyperfine splitting, one of the sidebands is again absorbed. For example, when the probe is tuned to about -10.2 GHz (-6.8 GHz detuned from the $|2\rangle$ resonance), the positive frequency sideband (red) is absorbed because it is generated at the frequency of the resonance. The negative frequency sideband (blue) is not absorbed because its frequency is far from resonance. However, its amplitude is reduced because the polarizability is inversely proportional to the optical detuning, as shown in the Supplemental Material [34]. In Fig. 3(c) we measure the sideband conversion efficiency versus number density. The conversion efficiency is equal to P_{s}/P_{c}, where P_{c} is the power of the probe before it enters the vapor cell, and P_{s} is the power of a particular sideband after leaving the cell. We set the probe frequency to be about halfway between the $|1\rangle$ and $|2\rangle$ resonances. The data and simulation of Fig. 3(b) indicate that the two sidebands should be the same amplitude for this probe detuning. However, the optical pumping was not 100% efficient in the experiment, and all the population was not initially in the $|2,2\rangle$ state. We found
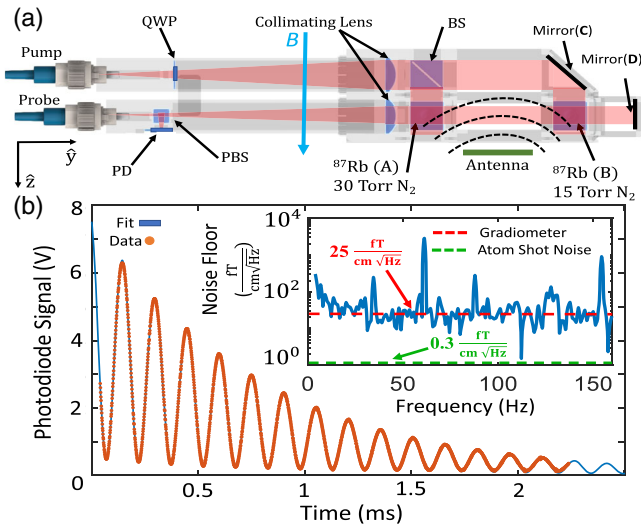
FIG. 4. (a) A schematic of the compact gradiometer sensor head. The probe makes two passes through vapor cells filled with ^{87}Rb vapor and nitrogen buffer gas. The sidebands are separated from the probe by the **PBS** and measured on a **PD**. (b) (Orange circles) **PD** output showing the beat note observed after applying a $\pi/2$ pulse. (Blue) Numerical fit to experimental data with Eq. (3). (Inset) Gradiometer noise floor obtained from the time series of beat-note frequencies in sequential cycles of gradiometer operation. Data was taken in an unshielded laboratory environment.

that to model this situation we could simply implement an imperfect $\pi/2$ pulse. Also, the model predicts the probe frequency was shifted 300 MHz towards $|1\rangle$ indicating we were not exactly between the two resonances. With about 60% of the atomic population remaining in the $|2, 2\rangle$ state after the microwave pulse, the model shows good agreement with the data. With an imbalance in population, one sideband is absorbed more quickly than the other as it propagates through the cell, and the model clearly predicts this behavior.

Guided by our tabletop experiments and numerical simulations, we developed a compact gradiometer sensor package. A schematic of our sensor package is shown in Fig. 4(a). The laser system is composed of two separate distributed feedback (DFB) lasers at 795 nm wavelength and resonant with the D1 transition. The lasers are coupled to the sensor head by a polarization maintaining (PM) optical fiber. A high-speed ($< 1 \mu s$) fiber-coupled electro-optical switch from Boston Applied Technologies (not shown) is used to switch the pump light on or off. The pump and probe beams are collimated to a 1 cm $1/e^2$ diameter. The probe passes through a polarizing beam splitter (**PBS**), and two cubic ($8 \times 8 \times 8$ mm^3 internal dimensions) ^{87}Rb vapor cells **A** and **B** separated by 4.4 cm. The pump is directed through the two cells in a direction orthogonal to the probe using a 50-50 nonpolarizing beam splitter (**BS**) and mirror (**C**).

In addition to ^{87}Rb, the vapor cells contain buffer gas with cell **A** nominally filled with 15 Torr of N_2 pressure and cell **B** nominally filled with 30 Torr of N_2 pressure. Heaters made from a flexible printed circuit board (not shown) are glued to the unused wall of the vapor cells to control the rubidium vapor pressure. A linearly polarized microstrip antenna is positioned between the two cells to apply a microwave $\pi/2$ pulse at frequency $\Delta\nu$ in Eq. (1). The probe, after passing through the two cells, is retroreflected using a gold-coated mirror (**D**) placed 2.2 cm away from the center cell **B**.

The distances between the cells (**A**, **B**) and the mirror (**D**) were carefully chosen to ensure constructive interference of the relative phase between the probe and sidebands for forward and backward propagating probe light. Maximum sideband generation occurs at integer spacings of the wavelength of the microwave radiation. This discrete spacing relative to the mirror gives a 2.2-cm spacing between the mirror and cell **A** and 6.6-cm spacing for the mirror to cell **B**, making the cell-to-cell separation (gradiometer baseline) 4.4 cm. After passing through the cells, the retroreflected light again passes through the **PBS** which directs the orthogonally polarized sideband light towards the **PD**.

The sensor is run in a pulsed mode with a 3 ms cycle time. During the first phase of the cycle (1.5 ms long), the pump light is switched on to spin polarize the atoms in both vapor cells. The pump laser wavelength is modulated at 200 kHz to be resonant with both the $5s^2S_{1/2}|1\rangle$ and $|2\rangle$ ground states to minimize hyperfine pumping and to transfer a majority of the atoms into the $|2, 2\rangle$ dark state. Because of limitations in the available pump optical power in the experiment (4 mW at the entrance of the sensor head), we estimate that roughly 60% of the atoms were optically pumped into the $|2, 2\rangle$ dark state in the two cells. After the optical pumping phase, the pump light is switched off and a $\pi/2$ pulse is applied to generate sidebands. The sideband light is separated from the probe light by the **PBS**, allowing only sideband light to pass to the **PD**.

Interference between the sideband light from the two vapor cells generates a beat note directly proportional to the gradient field between the two cells. Even in the absence of a significant gradient field, a beat-note with a 6 kHz frequency is observed due to the nominal 15 Torr differential in nitrogen buffer gas pressure between the two cells. The nitrogen buffer gas induced pressure shift for the ground state hyperfine transitions, $\Delta\nu_{BG}$, is approximately 548 Hz/Torr [37]. This offset frequency allows the gradiometer to function in a near zero-gradient field environment.

Since the beat note is produced by an interference of the electric fields from two exponentially decaying coherent light sources, the functional form of the photodiode output after the $\pi/2$ pulse is given by

$$S(t) = E_A^2 e^{-\frac{2t}{T_A}} + E_B^2 e^{-\frac{2t}{T_B}} + 2E_A E_B e^{-t(\frac{1}{T_A}+\frac{1}{T_B})} \sin(2\pi f t + \phi),$$
$$(3)$$

where E_A and E_B are the electric fields produced by the sidebands from cells **A** and **B**, respectively, T_A and T_B are the hyperfine ground state relaxation rates in the two cells, and $f = \Delta\nu_{BG} + 3\gamma|\Delta\mathbf{B}|$ is the relative frequency difference between the two sidebands (beat-note frequency). Considering $\Delta\nu_{BG}$ to be a constant offset, the magnitude of the magnetic field gradient between the two cells is obtained from a measurement of f. The zero gradient field frequency of the beat note was measured to be consistent with the known buffer gas pressure differential in the vapor cells used in our experiments. With the Earth's field oriented along z, the primary gradient measured is dB_z/dy. The raw photodiode output was digitized and recorded using a 16-bit, 2 MSPS analog-to-digital converter (ADC). In postprocessing, the beat-note obtained in each cycle was fitted to the functional form $S(t)$ to extract the beat-note frequency. As seen in Fig. 4(b), the fitted function closely overlaps with the experimental data. From the measurement of the beat-note frequency in each 3 ms cycle, a time series of the gradient field was obtained. From the Fourier transform of the gradient field time series, the gradiometer noise floor was calculated. Fig. 4(b) (inset) shows the gradiometer noise floor measured in the ambient laboratory background magnetic field to be 25 fT/cm/$\sqrt{\text{Hz}}$. An estimate of the atom shot noise (0.3 fT/cm/$\sqrt{\text{Hz}}$) from Eq. (1) in Ref. [38] is also shown. We expect the sensitivity to approach the atom shot noise limit by increasing the pump power to obtain unity spin polarization, improving the optics, and mitigating the technical noise. To improve the practical utility of our gradiometer, we also developed a second variant of the sensor package with colinear pump and probe beams that is described in the Supplemental Material [34].

In summary, we developed a novel method for direct optical observation of the magnetic field gradient between two spatially separated alkali vapor cells. The method relies on highly efficient sideband generation from the interaction between a linear probe beam and alkali atoms in a coherent superposition of magnetically sensitive hyperfine ground states. We developed a rigorous theoretical framework to accurately model our system and identify parameters to optimize its sensitivity. In addition, we demonstrate that our method is suitable for practical applications by developing an integrated, highly sensitive sensor package with readily available optical components. Because microwave sideband generation can be observed on all ground states in the hyperfine manifold that form a closed Λ system, the technique is suitable not only for magnetic sensing, but also for atomic clocks [24,25], radio-frequency sensing [39,40], and fundamental physics experiments [41,42].

The authors contributed in the following ways: Conceptualization: P. S., Y. J., I. S., V. S.; Tabletop experiments: K. C., Y. W.; Modeling and analysis: K. C., P. S., Y. W., Y. J.; Sensor design and construction: Y. W., V. S.; Theory: Y. J.; Letter writing: K. C., P. S., V. S.

---

[*] kccatfish93@unm.edu

[1] W. E. Bell and A. L. Bloom, Optical detection of magnetic resonance in alkali metal vapor, Phys. Rev. **107**, 1559 (1957).

[2] H. Dehmelt, Modulation of a light beam by precessing absorbing atoms, Phys. Rev. **105**, 1924 (1957).

[3] H. Tang and W. Happer, Parametric Frequency Conversion of Resonance Radiation in Optically Pumped Rubidium-87 Vapor, Phys. Rev. Lett. **24**, 551 (1970).

[4] I. Kominis, T. Kornack, J. Allred, and M. V. Romalis, A subfemtotesla multichannel atomic magnetometer, Nature (London) **422**, 596 (2003).

[5] H. Dang, A. C. Maloof, and M. V. Romalis, Ultrahigh sensitivity magnetic field and magnetization measurements with an atomic magnetometer, Appl. Phys. Lett. **97**, 151110 (2010).

[6] D. Budker and M. Romalis, Optical magnetometry, Nat. Phys. **3**, 227 (2007).

[7] T. M. Tierney, N. Holmes, S. Mellor, J. D. López, G. Roberts, R. M. Hill, E. Boto, J. Leggett, V. Shah, M. J. Brookes, R. Bowtell, and G. R. Barnes, Optically pumped magnetometers: From quantum origins to multi-channel magnetoencephalography, NeuroImage **199**, 598 (2019).

[8] V. K. Shah and R. T. Wakai, A compact, high performance atomic magnetometer for biomedical applications, Phys. Med. Biol. **58**, 8153 (2013).

[9] C. Johnson, P. D. D. Schwindt, and M. Weisend, Magnetoencephalography with a two-color pump-probe, fiber-coupled atomic magnetometer, Appl. Phys. Lett. **97**, 243703 (2010).

[10] M. Limes, E. Foley, T. Kornack, S. Caliga, S. McBride, A. Braun, W. Lee, V. Lucivero, and M. Romalis, Portable Magnetometry for Detection of Biomagnetism in Ambient Environments, Phys. Rev. Applied **14**, 011002(R) (2020).

[11] V. G. Lucivero, W. Lee, M. V. Romalis, M. E. Limes, E. L. Foley, and T. W. Kornack, Femtotesla nearly quantum-noise-limited pulsed gradiometer at earth-scale fields, arXiv:2112.09004.

[12] D. Cohen, Magnetoencephalography: Detection of the brain's electrical activity with a superconducting magnetometer, Science **175**, 664 (1972).

[13] J. E. Zimmerman and N. V. Frederick, Miniature ultrasensitive superconducting magnetic gradiometer and its use in cardiography and other applications, Appl. Phys. Lett. **19**, 16 (1971).

[14] R. H. Koch, J. R. Rozen, J. Z. Sun, and W. J. Gallagher, Three squid gradiometer, Appl. Phys. Lett. **63**, 403 (1993).

[15] K. Kamada, Y. Ito, S. Ichihara, N. Mizutani, and T. Kobayashi, Noise reduction and signal-to-noise ratio improvement of atomic magnetometers with optical gradiometer configurations, Opt. Express **23**, 6976 (2015).

[16] I. Sulai, Z. DeLand, M. Bulatowicz, C. Wahl, R. Wakai, and T. Walker, Characterizing atomic magnetic gradiometers for fetal magnetocardiography, Rev. Sci. Instrum. **90**, 085003 (2019).

[17] R. Zhang, R. Mhaskar, K. Smith, and M. Prouty, Portable intrinsic gradiometer for ultra-sensitive detection of magnetic gradient in unshielded environment, Appl. Phys. Lett. **116**, 143501 (2020).

[18] A. Perry, M. Bulatowicz, M. Larsen, T. Walker, and R. Wyllie, All-optical intrinsic atomic gradiometer with sensitivity in a 22 μt earth-scale magnetic field, Opt. Express **28**, 36696 (2020).

[19] V. G. Lucivero, W. Lee, N. Dural, and M. V. Romalis, Femtotesla Direct Magnetic Gradiometer Using a Single Multipass Cell, Phys. Rev. Applied **15**, 014004 (2021).

[20] E. Boto, N. Holmes, J. Leggett, G. Roberts, V. Shah, S. S. Meyer, L. D. Muñoz, K. J. Mullinger, T. M. Tierney, S. Bestmann *et al.*, Moving magnetoencephalography towards real-world applications with a wearable system, Nature (London) **555**, 657 (2018).

[21] A. Borna, T. R. Carter, A. P. Colombo, Y.-Y. Jau, J. McKay, M. Weisend, S. Taulu, J. M. Stephen, and P. D. Schwindt, Non-invasive functional-brain-imaging with an opm-based magnetoencephalography system, PLoS One **15**, e0227684 (2020).

[22] K. Jensen, M. A. Skarsfeldt, H. Stærkind, J. Arnbak, M. V. Balabas, S.-P. Olesen, B. H. Bentzen, and E. S. Polzik, Magnetocardiography on an isolated animal heart with a room-temperature optically pumped magnetometer, Sci. Rep. **8**, 1 (2018).

[23] K. Jensen, R. Budvytyte, R. A. Thomas, T. Wang, A. M. Fuchs, M. V. Balabas, G. Vasilakis, L. D. Mosgaard, H. C. Stærkind, J. H. Müller *et al.*, Non-invasive detection of animal nerve impulses with an atomic magnetometer operating near quantum limited sensitivity, Sci. Rep. **6**, 1 (2016).

[24] S. Knappe, V. Shah, P. D. Schwindt, L. Hollberg, J. Kitching, L.-A. Liew, and J. Moreland, A microfabricated atomic clock, Appl. Phys. Lett. **85**, 1460 (2004).

[25] J. C. Camparo, The rubidium atomic clock and basic research, Technical Report No. TR-2007(8555)-5, Aerospace Corporation, El Segundo, CA, Physical Sciences Laboratories, 2007.

[26] V. Gerginov, F. C. da Silva, A. Hati, and C. Nelson, An atomic sensor for direct detection of weak microwave signals, IEEE Trans. Microwave Theory Tech. **67**, 3485 (2019).

[27] A. Horsley and P. Treutlein, Frequency-tunable microwave field detection in an atomic vapor cell, Appl. Phys. Lett. **108**, 211102 (2016).

[28] H. Tang, Parametric frequency conversion of resonance radiation in optically pumped rb 87 vapor, Phys. Rev. A **7**, 2010 (1973).

[29] M. A. Rosenberry, J. P. Reyes, D. Tupa, and T. J. Gay, Radiation trapping in rubidium optical pumping at low buffer-gas pressures, Phys. Rev. A **75**, 023401 (2007).

[30] W. Happer, Optical pumping, Rev. Mod. Phys. **44**, 169 (1972).

[31] P. J. Oreto, Y.-Y. Jau, A. B. Post, N. N. Kuzma, and W. Happer, Buffer-gas-induced shift and broadening of hyperfine resonances in alkali-metal vapors, Phys. Rev. A **69**, 042716 (2004).

[32] Y.-Y. Jau, Spatial evolution of the multi-coherent light in alkali-metal vapor, an unpublished note for a density-matrix theory and numerical model to describe multitone light propagation in an atomic ensemble with nonzero atomic coherences. Please find the originally compiled note (June, 2007) "MLP1.pdf" in the Supplemental Material.

[33] W. Happer, Y.-Y. Jau, and T. Walker, *Optically Pumped Atoms* (Wiley-VCH, Weinheim, 2010).

[34] See Supplemental Material at http://link.aps.org/supplemental/10.1103/PhysRevLett.128.163602, which includes Refs. [9,32–36] for details about the theoretical model and colinear pump/probe operation of the gradiometer.

[35] D. Steck, Rubidium 87 d line data (2003).

[36] A. Ben-Kish and M. V. Romalis, Dead-Zone-Free Atomic Magnetometry with Simultaneous Excitation of Orientation and Alignment Resonances, Phys. Rev. Lett. **105**, 193601 (2010).

[37] J. Vanier, R. Kunski, N. Cyr, J. Savard, and M. Têtu, On hyperfine frequency shifts caused by buffer gases: Application to the optically pumped passive rubidium frequency standard, J. Appl. Phys. **53**, 5387 (1982).

[38] J. C. Allred, R. N. Lyman, T. W. Kornack, and M. V. Romalis, High-Sensitivity Atomic Magnetometer Unaffected by Spin-Exchange Relaxation, Phys. Rev. Lett. **89**, 130801 (2002).

[39] S.-K. Lee, K. Sauer, S. Seltzer, O. Alem, and M. Romalis, Subfemtotesla radio-frequency atomic magnetometer for detection of nuclear quadrupole resonance, Appl. Phys. Lett. **89**, 214106 (2006).

[40] I. M. Savukov, S. J. Seltzer, M. V. Romalis, and K. L. Sauer, Tunable Atomic Magnetometer for Detection of Radio-Frequency Magnetic Fields, Phys. Rev. Lett. **95**, 063004 (2005).

[41] T. Wang, D. F. J. Kimball, A. O. Sushkov, D. Aybas, J. W. Blanchard, G. Centers, S. R. O. Kelley, A. Wickenbrock, J. Fang, and D. Budker, Application of spin-exchange relaxation-free magnetometry to the cosmic axion spin precession experiment, Phys. Dark Universe **19**, 27 (2018).

[42] S. Afach, B. C. Buchler, D. Budker, C. Dailey, A. Derevianko, V. Dumont, N. L. Figueroa, I. Gerhardt, Z. D. Grujić, H. Guo *et al.*, Search for topological defect dark matter with a global network of optical magnetometers, Nat. Phys. **17**, 1396 (2021).